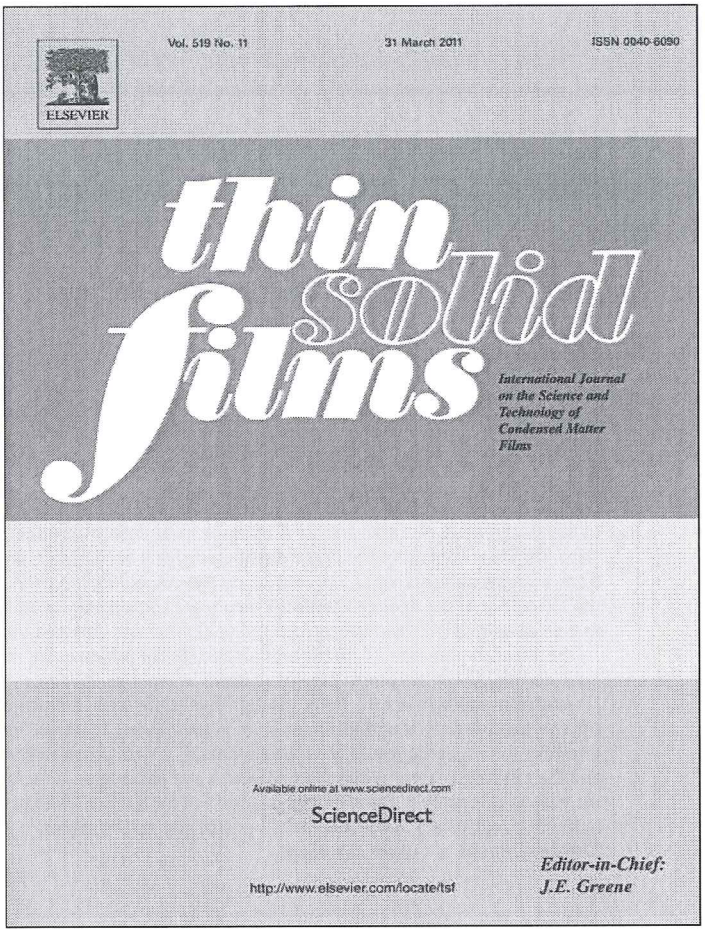

Thin Solid Films 519 (2011) 3745–3751

Contents lists available at ScienceDirect

Thin Solid Films

journal homepage: www.elsevier.com/locate/tsf

Atomic and electronic structure of both perfect and nanostructured Ni(111) surfaces: First-principles calculations

Sergei Piskunov [a,b,*], Guntars Zvejnieks [c], Yuri F. Zhukovskii [c], Stefano Bellucci [d]

[a] Faculty of Computing, University of Latvia, 19 Raina blvd., Riga LV-1586, Latvia
[b] Faculty of Physics and Mathematics, University of Latvia, 8 Zellu Str., Riga LV-1002, Latvia
[c] Institute for Solid State Physics, University of Latvia, 8 Kengaraga Str., LV-1063, Riga, Latvia
[d] INFN-Laboratori Nazionali di Frascati, Via Enrico Fermi 40, I-00044, Frascati, Italy

ARTICLE INFO

Article history:
Received 10 June 2010
Received in revised form 20 January 2011
Accepted 25 January 2011
Available online 2 February 2011

Keywords:
Ni(111) surface
Ni monomers
Ni dimers
Ni trimers
Ni nanoclusters
Density functional theory
Localized atomic orbitals
Plane waves

ABSTRACT

In this study, we perform first principles simulations on both atomically smooth and nanostructured Ni(111) slabs. The latter contains periodically distributed nickel nanoclusters atop a thin metal film gradually growing from adatoms and serving as a promising catalyst. Applying the generalized gradient approximation within the formalism of the density functional theory we compare the atomic and electronic structures of Ni bulk, as well as both perfect and nanostructured (111) surfaces obtained using two different *ab initio* approaches: (*i*) the linear combination of atomic orbitals and (*ii*) the projector augmented plane waves. The most essential inter-atomic forces between the Ni adatoms upon the substrate have been found to be formed *via*: (*i*) attractive pair-wise interactions, (*ii*) repulsive triple-wise interactions within a triangle and (*iii*) attractive triple-wise interactions within a line between the nearest adatoms. The attractive interactions surmount the repulsive forces, hence resulting in the formation of stable clusters from Ni adatoms. The magnetic moment and the effective charge (within both Mulliken and Bader approaches) of the outer atoms in Ni nanoparticles increase as compared to those for the smooth Ni(111) surface. The calculated electronic charge redistribution in the Ni nanoclusters features them as possible adsorption centers with increasing catalytic activity, *e.g.*, for further synthesis of carbon nanotubes.

1. Introduction

Nanostructured metallic films attract enhanced attention nowadays because of their unique properties that arise from the effects of size reduction and large number of interfaces. These films can be prepared using various methods, for example, sputtering, laser ablation, electro-deposition, nanolithography, etc. [1,2]. For uniform metallization of both non-planar and/or hidden surfaces, the methods of solution chemistry [3,4] are better suited than the physical vapor methods [5] since the former are not limited by the line-of-sight deposition. However, metal nanoclusters synthesized using the methods of solution chemistry are usually covered by hydroxide adsorbates [4]. This is why fabrication of pure Ni nanostructures was achieved using alternative techniques, *e.g.*, the electron-beam evaporation under the ultra-high vacuum (UHV) [5].

Nanostructured catalysts are very promising, in order to solve a number of the important technological problems in the future [6]. For example, the formation of Ni nanostructures acting as catalysts for the effective growth of carbon nanotubes is widely reported [7–9]. The model catalysts can be assembled as either a thin oxide film prepared over a metal substrate, thus avoiding its charging during the analysis performed by the electron spectroscopy methods (*e.g.* X-ray Photoelectron Spectroscopy), or metal particles deposited by evaporation with a tight distribution (± 1 nm) and size range 1–10 nm. The changes in the Ni substrate morphology, produced by three methods: (*i*) thermal evaporation and annealing of thin films, (*ii*) pulsed laser ablation and annealing of the nickel sample, and (*iii*) surface reactions of Ni-containing macromolecules, were studied using both atomic force microscopy and scanning electron microscopy [10,11]. In the case of thermal annealing of thin metal films in the temperature range 300–500 °C an increase in the mean diameter of the islands formed was observed, accompanied by a reduction in the mean island density with increasing temperature [10]. This effect was attributed to the mass transport of weakly bound individual Ni atoms and/or small island clusters across the surface, in order to form larger isolated islands. When using a pulsed KrF excimer laser for ablation of a Ni target, it was shown that the nm-smooth Ni thin films can be produced after a sufficient number of laser shots [11]. The surface morphology of these smooth films can be then altered by laser annealing that forms Ni droplets with diameter dependence on both the initial film thickness and the laser influence.

The Ni single crystal surfaces and their properties have been extensively studied over the last decades. The ferromagnetic nature of

* Corresponding author. Faculty of Computing, University of Latvia, 19 Raina blvd., Riga LV-1586, Latvia.
E-mail address: piskunov@lu.lv (S. Piskunov).

0040-6090/$ – see front matter © 2011 Elsevier B.V. All rights reserved.
doi:10.1016/j.tsf.2011.01.357

fcc Ni single crystal and its low-index surfaces was predicted from the results of *ab initio* calculations already in the 70s [12–14]. From first-principles, the structural, electronic and magnetic properties of perfect (001), (011), and (111) nickel surfaces have been thoroughly studied using generalized gradient approximation (GGA) corrected density functional theory (DFT) calculations performed within the formalism of either plane waves [15,16] or localized atomic orbitals [17]. Self-diffusion of Ni adatom upon the (111) and (001) nickel surfaces was examined both experimentally [18] and theoretically [19,20]. For Ni diffusion there were considered both Ni exchange [21] and transition-pathway model [22,23]. It was shown [24] that a regime of nickel thin film growth depends on the incident energy of adatoms and only for values exceeding 6 eV, the surface growth occurs through a layer-by-layer mechanism rather than an island growth mode. This can be attributed to the necessity for the 'smooth substrate' growth to overcome the large attraction energy of Ni–Ni surface atoms (estimated in this work to be 0.42 eV *per* pair) that favors a 3D cluster growth. In our earlier study, when combining both first-principles and thermodynamic approaches [25], we showed that the Cu clusters gradually growing on the MgO(001) substrate possess the shapes of sectioned pyramids.

In this paper, using two different first-principles DFT-GGA approaches based on the non-local Perdew–Burke–Erzernhof (PBE) Hamiltonian [26], *i.e.* the linear combination of atomic orbitals (LCAO) and the projector augmented plane waves (PAW), we discuss the atomic, electronic, and magnetic properties of the Ni(111) substrate covered by either adatoms or nanoclusters of nickel, as compared to atomically smooth Ni(111). The paper is organized as follows: Section 2 deals with computational details; the properties of Ni bulk and smooth (111) surface are analyzed in Section 3, the adsorption and association of nickel atom on a defectless substrate are considered in Section 4 while peculiarities of nanostructured Ni(111) are described in Section 5; Section 6 presents our main conclusions.

2. Computational details

In order to perform DFT-GGA-PBE LCAO spin-polarized calculations, we have used the *CRYSTAL-06* computer code [27]. Previously, we applied a similar computational formalism for the proper simulation on metallic surfaces (*e.g.*, both smooth densely-packed Al(111) and Al(001) as well as stepped Al(111) substrates and their interaction with oxygen [28]). In the current study, the Ni all-electron basis set (BS) has been employed: (8*s*–64111*sp*–41*d*) [29], with the exponents of core and valence shells being unchanged. In addition, the two virtual Ni *sp*-functions with exponents 0.63 and 0.13, respectively, and *d*-function with the exponent 0.38 have been used as optimized in bulk calculations [17]. To provide a balanced summation in direct and reciprocal lattices, the reciprocal space integration has been performed by sampling the Brillouin zone with the $2\times2\times1$ Monkhorst–Pack *k*-mesh [30], which results in 2 *k*-points in total for a 5×5 surface supercell of the Ni(111) substrate. Calculations are considered as converged only when the total energy differs by less than $2.7\cdot10^{-6}$ eV in two successive cycles of the self-consistence procedure. A smearing temperature of 315 K (0.001 a.u.) has been applied to the Fermi function. This value for the temperature has been chosen relatively low to ensure that the magnetic moment is not artificially modified by a too high value.

In our plane wave calculations on Ni(111) substrates, we have employed the scalar relativistic pseudopotentials combined with the PAW method [31], as implemented in the *VASP 4.6.36* code [32], in order to represent the core electrons (with the frozen semi-core states and 10 electrons in Ni pseudopotential). In these calculations, the PBE-GGA non-local functional [24] has been used for both exchange and correlation. We have used the Monkhorst–Pack scheme for generation of *k*-point mesh in reciprocal lattice (Γ-centered), which was set to $4\times4\times1$ in the case of 5×5 surface supercell. The cut-off energy has been optimized to be 400 eV while the vacuum gap has been chosen by such a way that the distance along the *z* axis between the top layers of the nanostructured surface has achieved 12 Å. Electronic relaxation is converged if the total energy differs less than 10^{-6} eV while the structural relaxation is completed if a modulus of all the forces acting on atoms is less than 0.001 eV/Å (this can be regulated by the input parameter EDIFFG [32]). We have used the second order Methfessel–Paxton smearing scheme for the partial occupancies [33] (with smearing parameter 0.15 eV) that has been found to be optimal for reasonable convergences suggesting the electronic entropy contribution of the order of 1 meV. Similar computational formalism was recently applied by us for the proper simulation on Au–Ni alloying upon the Ni(111) substrate [34].

3. Ni bulk and perfect Ni(111) surface

Before calculations of smooth and nanostructured Ni(111) we have verified the atomic and electronic structure of Ni bulk. Its calculated ground state properties are listed in Table 1. The optimized lattice parameters and atomic coordinates in the bulk unit cell obtained in the current study using both LCAO and PAW methods within DFT-GGA-PBE approach are close to experimentally obtained values. They qualitatively supplement each other although bulk modulus and cohesive energy calculated using the method of localized atomic orbitals are slightly overestimated as compared to the experiment, as usually observed when performing DFT calculations. On the other hand, the calculated value of magnetic moment for Ni bulk (0.62 μ_B obtained using both LCAO and PAW methods, Table 1) is in excellent agreement with its experimental value of 0.61 μ_B [36].

Periodic *ab initio* calculations on the crystalline surfaces are performed when considering a crystal as a stack of planes perpendicular to the surface and cutting out a 2D slab of finite thickness but periodic in the *x*–*y* plane. In *CRYSTAL-2006*, the PBE-GGA LCAO calculations on such a single slab are treated directly, whereas the plane wave calculations, in particular those performed using the *VASP* code, require translational symmetry along the *z* axis (repeating 3D slab model). In *VASP* PBE-GGA calculations on atomically smooth Ni(111) we have used a large enough vacuum gap about 20 Å between the periodically repeated 2D slabs. Table 2 presents the surface properties of perfect Ni(111). For relaxed slabs, the reference bulk unit cell energies were taken from the relaxed cubic cells. The calculation of the charge and spin population is based on the Mulliken population analysis [27] and Bader scheme [32]. The work function in LCAO calculations is obtained according to suggestion in [37], *i.e.*, a single layer of "ghost" functions [27] has been attached to the surface, to reproduce better a larger diffusivity of surface orbitals. Ni(111) surface properties obtained using both *ab initio* approaches applied in the present study are relatively close to each other, as well as they are in good agreement with results published previously (see Table 2). Based on this, we assume that our calculations on nanostructured Ni(111) yield reliable results too.

4. Association of Ni adatoms on perfect Ni(111) surface

In order to estimate the stability of Ni surface clusters we have calculated the interactions between Ni adatoms. In particular, the

Table 1
The properties of Ni bulk in the ground state as calculated using both LCAO and PAW DFT approaches: lattice constant a_0, bulk modulus B (evaluated by varying the lattice constant), cohesive energy E_{coh}, and magnetic moment M.

Method	a_0, Å	B, GPa	E_{coh}, eV	M, μ_B
GGA-PBE LCAO	3.532	203	5.01	0.62
GGA-PBE PAW	3.524	193	4.78	0.62
Experiment	3.52 [35]	190 [36]	4.44 [36]	0.61 [37]

Table 2
The atomic and electronic properties of perfect Ni(111) (5-layer slab model) calculated using both LCAO and PW methods: surface energy (cleavage energy with respect to bulk Ni) E_{surf}, work function W (experimental value 5.36 eV [38]), optimized distance D between different layers, effective charges Q on atoms located at different layers (using either LCAO or PAW approaches, respectively) and magnetic moment M for atoms at each layer.

Calculated values and units of their measurement	GGA-PBE LCAO[a]	GGA-PBE LCAO [17][b]	GGA-PBE PAW[c]	GGA-PBE PAW [15][d]
E_{surf}, J/m^2	0.13	0.12	0.10	0.10
W, eV	5.05	–	5.01	5.11
$D_{surf.-subsurf}$, Å	2.01	2.01	2.01	2.02
$D_{subsurf-3rd\text{-}layer}$, Å	2.04	–	2.03	2.04
Q_{surf}, e	0.056	–	0.029	–
$Q_{subsurf}$, e	−0.055	–	−0.023	–
$Q_{3rd\text{-}layer}$, e	−0.001	–	−0.012	–
M_{surf}, μ_B	0.68	0.65	0.61	0.68
$M_{subsurf}$, μ_B	0.66	0.66	0.63	0.65
$M_{3rd\text{-}layer}$, μ_B	0.65	0.62	0.61	0.62

[a] For 11×11×1 Monkhorst–Pack k-mesh.
[b] 9-layer slab.
[c] For 13×13×1 Monkhorst-Pack k-mesh.
[d] 9-layer slab, 3 central layers have been fixed during relaxation.

interaction energy for a given configuration of m adatoms can be obtained from the first-principles (FP) calculations [39]:

$$E^{FP} = (E_m - E_0) - m\left(E_1^{Ni} - E_0\right), \quad (1)$$

where E_m is the total slab energy (including m adatoms), E_1^{Ni} the total energy of slab containing a single Ni adatom, and E_0 the total energy of a bare slab. On the other hand, lattice gas (LG) Hamiltonian for such a configuration can be written as [40]:

$$E^{LG} = \frac{1}{2!}\sum\nolimits'_{ij} v_{ij}^{pair} n_i n_j + \frac{1}{3!}\sum\nolimits'_{ijk} v_{ijk}^{trio} n_i n_j n_k + \ldots, \quad (2)$$

where $n_\alpha = 1$ if the site α (i,j,k) is occupied and 0 in opposite cases. Indices j and k run over all the sites while i is limited to the original supercell; prime at summation symbol in Eq. (2) denotes that self-interaction is excluded. Under *hypothesis* that the interactions are additive one can equate $E^{FP} \equiv E^{LG}$. In this study we limit ourselves to pair- and triple-wise interactions only, see Eq. (2). When selecting at least as many different non-equivalent surface configurations (Fig. 1a–f) as the interaction constants exist, we obtain a set of linearly independent equations that contain unknown interaction constants v (Tables 3 and 4) and the corresponding configuration interaction energies E^{FP} obtained from the first-principles calculations.

Table 3
Pair-wise interactions v_i (eV) (subscript index i denotes first, second and third NN interactions) for different number of layers in slabs.

Slab model	v_1	v_2	v_3
Pair, 3-layer	−0.37 ± 0.06	0.017 ± 0.007	0.013 ± 0.013
Pair, 5-layer	−0.42 ± 0.03	0.016 ± 0.003	0.009 ± 0.007

First, we have calculated the pair-wise interactions v^{pair} up to the 3rd nearest neighbor (NN) distances indicated by the subscript v_1, v_2 or v_3, respectively. For pair interaction calculations, we have used configurations similar to those suggested in Ref. [40] and shown in Fig. 1a–b–c. In order to exclude the slab effect, we have simulated adatom configurations located upon: (*i*) 3-layer asymmetric slab with the fixed bottom layer of Ni atoms in their bulk-like positions, while the two next layers with surface adatoms have been allowed to relax (in this limit we have used 430 eV cut-off energy and 13×13×1 Monkhorst–Pack k-point mesh [30]); (*ii*) 5-layer symmetric slab with adatoms placed on both slab sides; in this case, all the atoms have been allowed to relax, while cutoff and k-point mesh has decreased to 320 eV and 8×8×1, respectively. Structural relaxation in this case has been terminated if a modulus of all the forces acting on atoms is less 0.01 eV/Å. It has been shown that the number of layers has practically no effect on pair-wise interactions between Ni adatoms (Table 3) while the limits of estimated error (when assuming that the energy of each configuration is determined up to precision of 10 meV) have decreased twice. This is due to the fact that the number of adatom configurations in symmetric case (*ii*) has increased twice. The distance between the Ni adatoms in a pair (Fig. 1c) is contracted to 2.36 Å (Table 5), as compared to 2.49 Å distance between the NN atoms at a clean surface. This contraction is caused by a strong Ni–Ni attraction (−0.42 eV as obtained for the 5-layer slab). At the same time we have observed weak repulsions between adatoms located at 2nd and 3rd NN positions which decrease with a distance.

Next, we have considered the following triple-wise interactions v^{trio}: trio in a triangle, v_{tt} (Fig. 1d), bent trio, v_{tb} (Fig. 1e), and trio in a line, v_{tl} (Fig. 1f). The triple-wise interaction energies obtained with these configurations for both 3- and 5-layer slabs are given in Table 4 and denoted as low adatom concentration interactions (Trio-L),

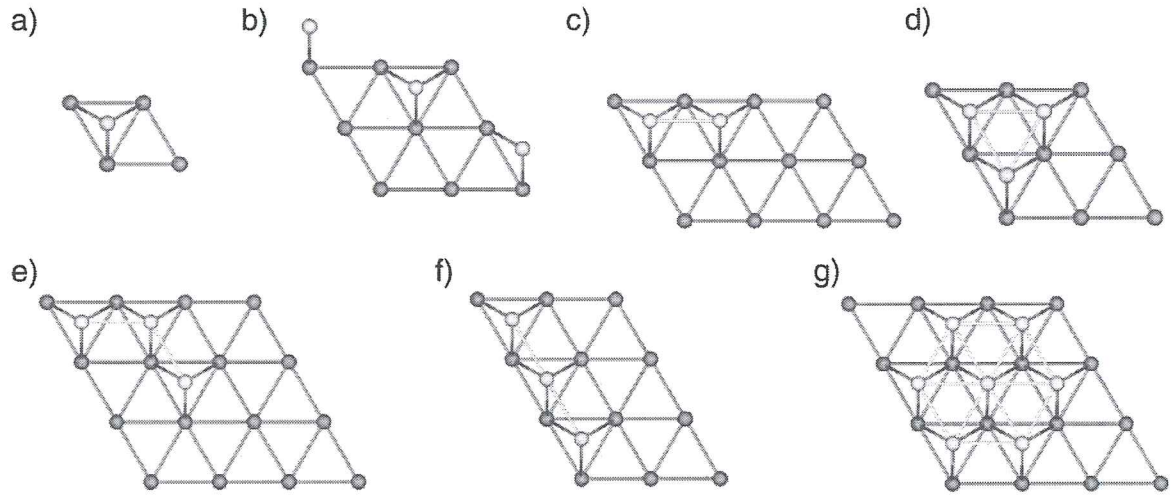

Fig. 1. Supercell top views of different Ni adatom configurations (yellow circles) upon Ni(111) surface atoms (scarlet circles). Different adatom configurations (a)–(f) are used to determine the Ni–Ni interaction energies, while configuration (g) is used as a test case (see the last paragraph of Section 4 for details). (For interpretation of the references to color in this figure legend, the reader is referred to the web version of this article.)

Table 4
Triple-wise interactions (eV) for high (Trio-H) and low (Trio-L) adatom concentration C (Table 5) and different number of layers in slabs.

Slab model	v_{tt}	v_{tb}	v_{tl}
Trio-H 3-layer	0.17 ± 0.15	-0.04 ± 0.04	-0.07 ± 0.09
Trio-L 3-layer	0.14 ± 0.18	-0.03 ± 0.12	-0.11 ± 0.09
Trio-L 5-layer	0.14 ± 0.09	-0.04 ± 0.04	-0.07 ± 0.04

since $C<0.5$. As in the case of pair-wise interactions, all energies are rather insensitive to the thickness of the slab. We detect that trio in a triangle configuration (Fig. 1d) shows a strong repulsion of 0.14 eV and increase of the pair distance between the adatoms up to 2.40 Å (Table 5). The triple-wise interaction in a bent position is negligible and the distance between adatom pairs practically coincides with the NN pair distance. Trio in a line configuration demonstrates moderate attraction that has no effect on the inter-particle distances. Since the choice of adatom configurations is not unique, the triple-wise interactions can also be calculated for configurations with a high adatom concentration (Trio-H), $C \geq 0.5$ (see Fig. 1 in Ref. [40]), with a higher symmetry. In this case trio in a triangle repulsion is larger, but all NN distances between adatoms are equal to 2.49 Å (Tables 4 and 5). All calculated triple-wise interactions coincide within the error limits. However, the discrepancy can be attributed to higher order interactions, see infinite sum of terms in Eq. (2), that are present in Ref. [40] configurations due to periodic boundary conditions, but are unaccounted in our pair and trio interaction model.

Verification for the 3-layer asymmetric slab has been done, from the one side, by calculating the configuration (Fig. 1g) interaction energy *per* adatom $E^{FP}/m = -0.62 \pm 0.03$ eV, using the first-principles calculations according to Eq. (1). On the other hand, we calculate energy from the LG Hamiltonian, Eq. (2), using the determined interaction energies from Tables 3 and 4 at low concentration limit and obtain: $E^{LG}/m = -0.58 \pm 0.25$ eV. Both results practically coincide within the error limits.

Relaxation of the surface in the case of a *single* Ni atom adsorption is rather ordinary: the three nearest surface atoms both (*i*) move away from their equilibrium positions (by 0.04 Å) along in-plane radial directions (*XY*) and (*ii*) rise slightly (by 0.01 Å) in a direction perpendicular to the surface (*Z*). The distance from adatom to these surface atoms relaxes to 2.30 Å. A similar case is observed for adsorbed *dimer* (Fig. 2a): all the nearest substrate atoms move away from it. Each surface atom (A), which is a nearest neighbor for both dimer adatoms, relaxes away in-plane by ≤ 0.05 Å from its equilibrium position being pushed down into the substrate by -0.02 Å in the *Z* direction. The distance from this atom to adatoms of dimer rises up to 2.33 Å. Other four nearest surface atoms relax by ~0.03 Å away and rise up by 0.02 Å from their equilibrium positions (Fig. 2a). This reduces the distances between the corresponding adatoms and the nearest surface atoms (B, which are in NN positions) down to 2.30 Å. The distance to the remaining two surface atoms (C, which are the most remote) is increased up to 2.38 Å since the separation between dimer atoms is contracted down to 2.36 Å. In the case of a *triangle* adatom adsorption (Fig. 2b) the surface atom, which has all three adatoms as nearest neighbors, is shifted downwards in the *Z* direction by -0.06 Å while having no in-plane relaxation. As to other six surface atoms nearest to the trimer, they relax away by 0.03 Å in-plane and rise up by 0.03 Å along the *Z* direction. In this case, the distance between each adatom and its nearest surface atoms equals to 2.37 Å.

Table 5
Dependence of inter-particle distance (Å) on adatom configuration and concentration.

Concentration	Pair	Trio in a triangle	Trio bent	Trio in a line
Low, $C<0.5$	2.36	2.40	2.36	2.37
High, $C \geq 0.5$	–	2.49	2.49	2.49

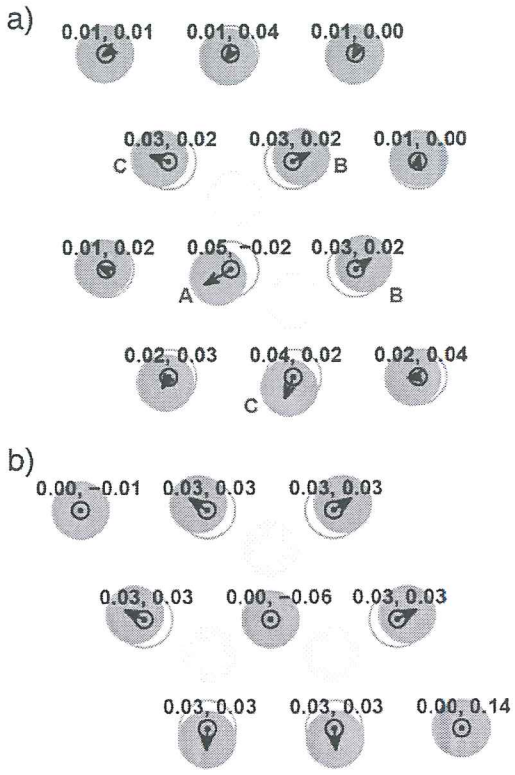

Fig. 2. Relaxation of Ni surface atoms (light scarlet circles) caused by dimer (a) and trimer (b) formed from Ni adatoms (light yellow circles) as compared to the initial surface atom positions (open circles). In-plane directions of surface atom relaxations (*XY*) are marked by arrows and their absolute values (in Å) are given as first in number pairs, while the second numbers indicate relaxations in direction perpendicular to the surface (*Z*) pointing upwards. (For interpretation of the references to color in this figure legend, the reader is referred to the web version of this article.)

Let us analyze the evolution of Ni adatom positions when gradually growing the nanostructure (Fig. 1). Firstly, the distance of 2.40 Å between the adatoms in trio-triangle configuration (Fig. 1d) is increased as compared to the distance 2.36 Å in a pair (Fig. 1c). Next, a further increase of surface atom concentration for configuration shown in Fig. 1g leads to a Ni–Ni distance of 2.42 Å. Finally, the two-layer Ni nanocluster shown in Fig. 3 is obtained by placing the three additional adatoms atop the seven-adatom configuration (Fig. 1g). This results in a further increase of the inter-atom distance within the first adatom layer to 2.46 Å, that practically reaches a value of 2.49 Å for Ni–Ni distance in the (111) plane. Meanwhile, the distance between the top 3 adatoms is equal to 2.39 Å that is comparable to the pair distances of 2.40 Å in trio-triangle configuration (Fig. 1d).

In order to explain the atom-projected density of states (DOS) calculated for monomer, dimer and triangle adatom configurations (Fig. 4), we additionally use information about the Bader charge distribution and structural relaxation. In the case of monomer adsorption, the electronic charge is transferred from the adatom towards the surface layer of slab (-0.057 *e*), which is almost twice as larger than that transferred from the surface atom of the smooth (111) surface towards the subsurface layer (-0.029 *e*, Table 2). Since the single Ni adatom is positively charged as compared to the surface it can be more strongly attracted by slab atoms, which results in a reduced distance of 2.30 Å between the adatom and three nearest surface atoms. The proximity of these atoms causes an increase of the

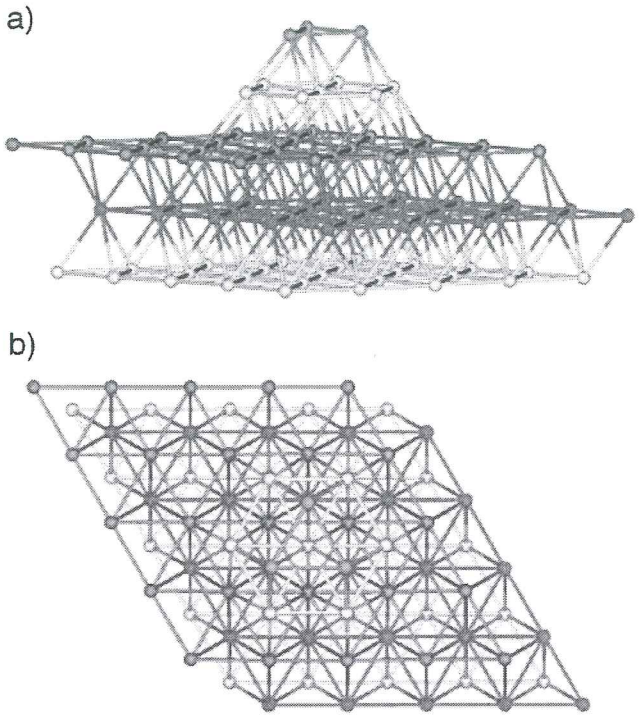

Fig. 3. Schematic illustration of supercell for the nanostructured Ni(111) slab: (a) side view and (b) top view. Each surface plane is shown by different colors (grayscale halftones) as a guide to eyes. The lower (light-blue) plane is a mirror plane of the symmetrically terminated 5-layer slab. (For interpretation of the references to color in this figure legend, the reader is referred to the web version of this article.)

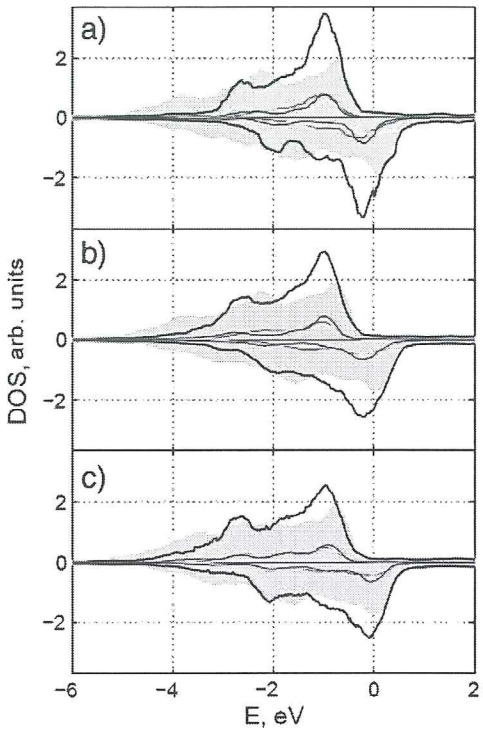

Fig. 4. The total density of states (grey-filled areas), the atom-projected DOS (bold black lines) and the atom-angular-momentum-projected densities of *d*-states: red (semi-dark) lines for d_{xy} and $d_{x^2-y^2}$ orbitals, yellow (light) lines for d_{yz} and d_{xz} orbitals, as well as blue (dark grey) lines for $d_{3z^2-r^2}$ orbital) calculated for Ni monomer (a), dimer (b) and triangle trimer (c) adsorbed upon the Ni(111) substrate. All the DOS are calculated per atom. (For interpretation of the references to color in this figure legend, the reader is referred to the web version of this article.)

projected DOS for monomer adatom (Fig. 4a), due to a Pauli principle of exclusion. The main contributions to the increased DOS come from d_{xy} (which is equivalent to $d_{x^2-y^2}$) and $d_{3z^2-r^2}$ orbitals of adatom while the influence of d_{yz} orbital (which is equivalent to d_{xz}) is almost unchanged for different concentrations of adatoms. In the case of dimer adsorption, the charge transferred to the slab is smaller than that from monomer (−0.036 *e* averaged *per* adatom) and the distance between adatoms and surface atoms ranges from 2.30 to 2.38 Å. This is why, although the profiles of projected DOS for dimer (Fig. 4b) are qualitatively similar to those for monomer (Fig. 4a), the main contributions to the former come from $d_{3z^2-r^2}$ orbitals, while the densities of d_{xy} states decrease reaching the level of d_{yz}, thus reducing the densities of projected DOS. The charge transferred to the slab from a triangle of NN adatoms (−0.033 *e per* adatom) is smaller than that from a dimer, while the distances between adatoms and surface atoms equal to 2.37 Å. As a result, the projected DOS of triangle trimer (Fig. 4c) is smaller than those for monomer (Fig. 4a) and dimer (Fig. 4b), while the contribution of $d_{3z^2-r^2}$ orbital reaches the level of other *d*-orbital projections. Further growth of the nanocluster formed by adatoms leads to further approach of the projected DOS to the total DOS of the nanostructured slab (for the 10-atom cluster shown in Fig. 3 both DOS almost coincide).

The most relevant inter-atomic forces connecting the Ni adatoms upon the substrate are: (*i*) attractive pair-wise interactions in NN pairs (−0.42 eV), (*ii*) repulsive triple-wise interactions within NN triangles (0.14 eV) and (*iii*) attractive triple-wise interactions within a line between NN adatoms (−0.07 eV). Repulsive character of triple-wise interactions within triangles can be explained by additivity hypothesis, when $E^{FP} \equiv E^{LG}$, see also Eqs. (1)–(2), thus, trio interactions have to compensate the strong attractive pair-*wise* interactions. On the other hand, adsorption of Ni monomer and dimer involves slightly different chemical binding, due to *d*-orbital overlap effects, which are absent in the case of trio in a triangle. When the localization of interfacial atoms is insufficient to form a quasi-molecule the additivity hypothesis holds.

Thus, the attractive interactions surmount the repulsive inter-atomic forces and results in a formation of stable Ni clusters on the

Table 6
The atomic and electronic properties of the nanostructured Ni(111) slab calculated using LCAO and PW methods (see details in caption of Table 2). Formation energy E_{form} with regard to Ni bulk is calculated *per* number of atoms in the slab unit cell, while $E_{form-surf}$ is a cleavage energy with regard to Ni bulk. Values *Q* and *M* are averaged *per* layer atom.

Calculated values and units of their measurement	GGA-PBE LCAO	GGA-PBE PW[a]
E_{form}, J/m^2	0.03	0.03
$E_{form-surf}$, J/m^2	0.03	0.02[b]
W, eV	4.30	4.42
$D_{nano-top-middle}$, Å	1.87	1.90
$D_{nano-middle-surf.}$, Å	1.92	1.90
$D_{surf.-subsurf.}$, Å	2.04	2.02
$D_{subsurf.-central}$, Å	2.00	2.02
$Q_{nano-top}$, *e*	+0.142	+0.032
$Q_{nano-middle}$, *e*	+0.004	−0.040
$Q_{surf.}$, *e*	+0.013	+0.024
$Q_{subsurf.}$, *e*	−0.030	−0.016
$Q_{central}$, *e*	−0.002	0.000
$M_{nano-top}$, μ_B	0.85	0.84
$M_{nano-middle}$, μ_B	0.72	0.74
$M_{surf.}$, μ_B	0.67	0.66
$M_{subsurf.}$, μ_B	0.66	0.66
$M_{central}$, μ_B	0.62	0.63

[a] For 4×4×1 Monkhorst-Pack *k*-mesh.
[b] For 13×13×1 Monkhorst-Pack *k*-mesh.

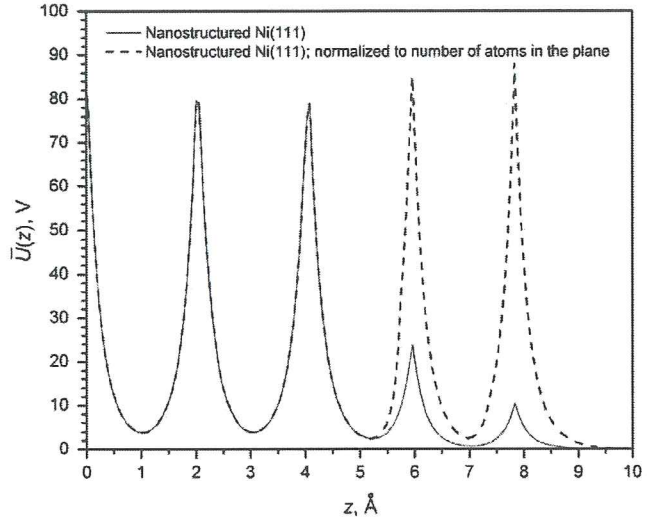

Fig. 5. Distributions of the in-plane averaged electrostatic potential $\bar{U}(z)$ across the 5-layer slab model of the nanostructured Ni(111) surface. Zero on the z-axis corresponds to the central layer of the slab (mirror plane).

surface. Meanwhile, in-plane distance between the adatoms within the growing surface clusters by deposition of a second adatom layer practically reaches its value in Ni bulk.

5. Nanostructured Ni(111) surface

The supercell of the three-layer slab for the nanostructured Ni(111) substrate is shown in Fig. 3. Nanoparticle atop the perfect Ni(111) is modeled here adding seven and three Ni atoms in the corresponding positions of the 4th and 5th layers, respectively. Table 6 presents the properties of the nanostructured Ni(111) surface. Its formation energy is larger as compared to the corresponding value for the perfect surface (Table 2) while the work function is reduced, due to a larger number of facets. The nearest interlayer distances in the surface Ni nanocluster are significantly smaller than those in the smooth surface slab. According to the Mulliken analysis, nickel atoms from the nanocluster's tip gain additionally 0.142 *e*. The magnetic moments of the nanocluster are strongly enhanced (up to 0.85 μ_B) with respect to the magnetic moments within the smooth surface (~0.62 μ_B). Predicted high-moment state of the surface nanocluster agrees well with the increase of spin density suggested recently for Ni nanowires and nanorods [41]. On the whole, we can observe qualitative agreement of results calculated using both LCAO and PAW methods.

When estimating the surface properties we should take into account the vertical distribution of two-dimensional average electrostatic potentials [17] across the slab:

$$\bar{U}(z) = \frac{1}{S}\int_S U(x,y,z)dxdy \tag{3}$$

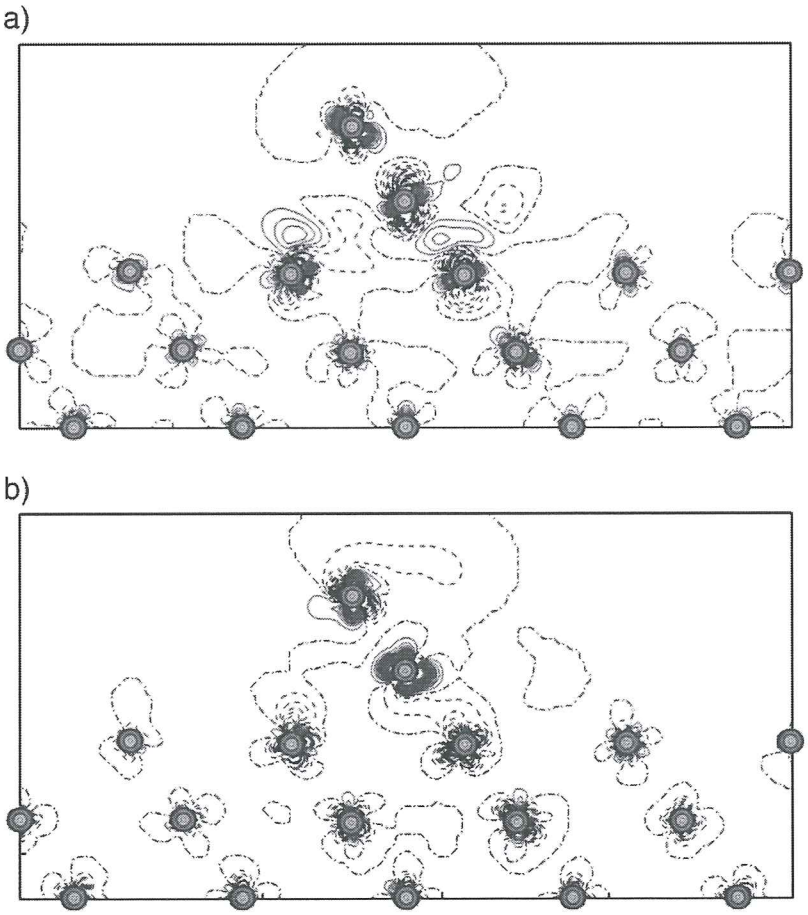

Fig. 6. The calculated (110) cross-sections of the electron (a) and spin (b) density redistributions $\Delta\rho(\mathbf{r})$ corresponding to a difference between the total density for the nanostructured Ni(111) slab and the sum of total densities for the perfect Ni(111) slab and separated surface nanocluster, respectively. Dash–dot (black) isolines correspond to the zero level. Dashed (blue) isolines stand for a decrease in $\Delta\rho(\mathbf{r})$ and solid (red) lines for an increase. Isodensity curves are drawn from −0.05 to +0.05 e a.u.$^{-3}$ with an increment of 0.00167 e a.u.$^{-3}$. (For interpretation of the references to color in this figure legend, the reader is referred to the web version of this article.)

where S is the total area of a surface unit cell. Using Eq. (3), we construct the potential distributions for both smooth and nanostructured Ni slabs (Fig. 5). Surface relaxation has no substantial influence on the distribution of the electrostatic potential across the surface unit cell of the perfect slab. The most drastic changes occur at the Ni nanocluster (4th and 5th layers) where one can observe the marked differences between the $\overline{U}(z)$ distributions for nanostructured and smooth slabs, while the potentials of the internal atomic layers inside the Ni(111) slab remain almost unchanged. Analogous effect was observed for the stepped Al(111) substrate simulated by us earlier [28] which was found to be considerably more active towards the interaction with the oxygen adsorbate than a smooth substrate. Thus, from the calculated distributions of electrostatic potential (Fig. 5) we can predict a noticeable growth of catalytic activity in the case of the nanostructured Ni(111) surface.

Both electronic charge and spin redistributions across the nanostructured Ni(111) slab (Fig. 6) clearly show an increase of their densities towards the tip of the nanocluster implying that it can be an effective adsorption center, due to a reduction of the coordination number of its atoms. We can observe a noticeable redistribution of the electronic density (Fig. 6a) around the Ni nanocluster. This causes a strong polarization of the corresponding atoms, without considerable charge transfer across the boundary between the smooth slab and nanocluster (Table 6). On the other hand, Fig. 6b shows a substantial transfer of the spin density towards the nanocluster's tip which can be explained by the enhanced values of magnetic moments at corresponding Ni atoms (Table 6). Obtained results give a preference for the Ni nanoclusters as effective sites for adsorption and catalysis as compared to the smooth Ni(111) areas.

6. Conclusions

In this study, we have performed the large-scale first-principles calculations on both atomically smooth and nanostructured Ni(111) slabs. We have shown that the gradual homogeneous adsorption of Ni atoms on the nickel substrate results in the formation of stable Ni surface nanoclusters. Using both LCAO and PAW approaches, we predict both increase of the magnetic moment and strong polarization on the outer atoms of Ni nanoclusters as compared to the smooth Ni(111). The calculated electronic charge and spin density redistributions around the Ni nanoclusters feature them as active adsorption complexes applicable in different technological developments [6]. Such a nanostructured thin metal film can act as a promising catalyst for further synthesis of carbon nanotubes [7–9]. Qualitatively adequate theoretical description of the nanostructured Ni catalyst is crucial for the proper simulation of CNT growth that is currently in progress.

Acknowledgements

This study has been partly supported by EC FP7 CATHERINE project. S.P. and G.Z. greatly acknowledge the financial support through ESF projects 2009/0216/1DP/1.1.1.2.0/09/APIA/VIAA/044 and 2009/0202/1DP/1.1.1.2.0/09/APIA/VIAA/141, respectively.

References

[1] H.V. Jansen, N.R. Tas, J.W. Berenschot, in: H.S. Nalwa (Ed.), Encyclopedia of Nanoscience and Nanotechnology, vol. 5, American Scientific Publishers, 2004, p. 163.
[2] C.C. Baker, A. Pradhan, S. Ismat Shah, in: H.S. Nalwa (Ed.), Encyclopedia of Nanoscience and Nanotechnology, vol. 5, American Scientific Publishers, 2004, p. 449.
[3] Z. Libor, Q. Zhang, Mater. Chem. Phys. 114 (2009) 902.
[4] H. Wang, D.O. Northwood, J. Mater. Sci. 43 (2008) 1050.
[5] K. Venkataramani, S. Helveg, B. Hinnemann, M. Reichling, F. Besenbacher, J.V. Lauritsen, Nanotechnology 21 (2010) 265602.
[6] Q. Wang, A.E. Ostafin, in: H.S. Nalwa (Ed.), Encyclopedia of Nanoscience and Nanotechnology, vol. 5, American Scientific Publishers, 2004, p. 475.
[7] H. Dai, A.G. Rinzler, P. Nikolaev, A. Thesi, D.T. Colbert, R.E. Smalley, Chem. Phys. Lett. 260 (1996) 471.
[8] S. Reich, L. Li, J. Robertson, Chem. Phys. Lett. 421 (2006) 469.
[9] S. Hofmann, R. Sharma, C. Ducati, G. Du, C. Mattevi, C. Cepek, M. Cantoro, S. Pisana, A. Parvez, F. Cervantes-Sodi, A.C. Ferrari, R. Dunin-Borkowski, S. Lizzit, L. Petaccia, A. Goldoni, J. Robertson, Nano Lett. 7 (2007) 602.
[10] J.D. Carey, L.L. Ong, S.R.P. Silva, Nanotechnology 14 (2003) 1223.
[11] S.J. Henley, C.H. Poa, D.A. Addikaari, C. Giusca, J.D. Carey, S.R.P. Silva, Appl. Phys. Lett. 84 (2004) 4035.
[12] C.S. Wang, J. Callaway, Phys. Rev. B 9 (1974) 4897.
[13] R. Dovesi, C. Pisani, C. Roetti, Surf. Sci. 103 (1981) 482.
[14] W. Hübner, Phys. Rev. B 42 (1990) 11553.
[15] F. Mittendorfer, A. Eichler, J. Hafner, Surf. Sci. 423 (1999) 1.
[16] M. Gajdos, A. Eichler, J. Hafner, J. Phys. Condens. Matter 16 (2004) 1141.
[17] K. Doll, Surf. Sci. 544 (2003) 103.
[18] T.Y. Fu, T.T. Tsong, Surf. Sci. 454–456 (2000) 571.
[19] U. Kürpick, Phys. Rev. B 64 (2001) 075418.
[20] U. Kürpick, Phys. Rev. B 66 (2002) 165431.
[21] H. Bulou, C. Massobrio, Phys. Rev. B 72 (2005) 205427.
[22] S.Y. Kim, I.H. Lee, S. Jun, Phys. Rev. B 76 (2007) 245407.
[23] S.Y. Kim, I.H. Lee, S. Jun, Phys. Rev. B 76 (2007) 245408.
[24] S.G. Lee, Y.C. Chung, Appl. Surf. Sci. 253 (2007) 8896.
[25] D. Fuks, E.A. Kotomin, Yu.F. Zhukovskii, A.M. Stoneham, Phys. Rev. B 74 (2006) 115418.
[26] J.P. Perdew, K. Burke, M. Ernzerhof, Phys. Rev. Lett. 77 (1996) 3865.
[27] R. Dovesi, V.R. Saunders, C. Roetti, R. Orlando, C.M. Zicovich-Wilson, F. Pascale, B. Civalleri, K. Doll, N.M. Harrison, I.J. Bush, Ph. D'Arco, M. Llunell, CRYSTAL-2006 User's Manual, University of Torino, Torino, 2006, http://www.crystal.unito.it/.
[28] Yu.F. Zhukovskii, P.W.M. Jacobs, M. Causà, J. Phys. Chem. Solids 64 (2003) 1317.
[29] M.D. Towler, N.L. Allan, N.M. Harrison, V.R. Saunders, W.C. Mackrodt, E. Aprà, Phys. Rev. B 50 (1994) 5041.
[30] H.J. Monkhorst, J.D. Pack, Phys. Rev. B 13 (1976) 5188.
[31] P.E. Bloechl, Phys. Rev. B 50 (1994) 17953.
[32] G. Kresse, M. Marsman, J. Furthmüller, VASP the Guide, University of Vienna, Austria, 2009, http://cms.mpi.univie.ac.at/vasp/vasp/vasp.html.
[33] M. Methfessel, A.T. Paxton, Phys. Rev. B 40 (1989) 3616.
[34] G. Zvejnieks, E.E. Tornau, Proceedings of the 14th International Conference on Thin Films, Ghent, Belgium, November 17–20, 2008, p. 358.
[35] K.A. Gschneidner Jr., Solid State Phys. 16 (1964) 276.
[36] C. Kittel, Introduction to Solid State Physics, Wiley, New York, Chichester, Brisbane, Toronto, Singapore, 1996.
[37] K. Doll, Surf. Sci. 600 (2006) L321.
[38] H.B. Michaelson, J. Appl. Phys. 48 (1977) 4729.
[39] K.A. Fichthorn, M. Scheffler, Phys. Rev. Lett. 84 (2000) 5371.
[40] C. Stampfl, H.J. Kreuzer, S.H. Payne, H. Pfnür, M. Scheffler, Phys. Rev. Lett. 83 (1999) 2993.
[41] M. Zeleny, M. Sob, J. Hafner, Phys. Rev. B 79 (2009) 134421.